

Defect emission and its dipole orientation in layered ternary ZnIn₂S₄ semiconductor

Rui Wang^{1,Δ}, Quan Liu^{3,Δ}, Sheng Dai⁵, Chao-Ming Liu^{1,7}, Yue Liu¹, Zhao-Yuan Sun¹, Hui Li⁴, Chang-Jin Zhang⁴, Han Wang^{5,*}, Cheng-Yan Xu⁵, Wen-Zhu Shao^{1,*}, Alfred J. Meixner³, Dai Zhang^{3,*}, Yang Li^{1,2,*} and Liang Zhen^{1,2,6}

¹ School of Materials Science and Engineering, Harbin Institute of Technology, Harbin 150001, China

² MOE Key Laboratory of Micro-Systems and Micro-Structures Manufacturing, Harbin Institute of Technology, Harbin 150080, China

³ Institute of Physical and Theoretical Chemistry, Eberhard Karls University Tübingen, Tübingen 72076, Germany

⁴ School of Physical Science and Technology, Center for Transformative Science, ShanghaiTech University, Shanghai 201210, China

⁵ Institutes of Physical Science and Information Technology, Anhui University, Hefei 230601, China

⁶ Sauvage Laboratory for Smart Materials, School of Materials Science and Engineering, Harbin Institute of Technology (Shenzhen), Shenzhen 518055, China

⁷ Laboratory for Space Environment and Physical Sciences, Harbin Institute of Technology, 150001 Harbin, China

E-mails: liyang2018@hit.edu.cn (Y.L.); wzshao@hit.edu.cn (W.Z.S.); wanghan3@shanghaitech.edu.cn (H.W.); dai.zhang@uni-tuebingen.de (D.Z.)

Abstract: Defect engineering is promising to tailor the physical properties of two-dimensional (2D) semiconductors for function-oriented electronics and optoelectronics. Compared with the extensively studied 2D binary materials, the origin of defects and their influence on physical properties of 2D ternary semiconductors have not been clarified. In this work, we thoroughly studied the effect of defects on the electronic structure and optical properties of few-layer hexagonal ZnIn_2S_4 via versatile spectroscopic tools in combination with theoretical calculations. It has been demonstrated that the Zn-In anti-structural defects induce the formation of a series of donor and acceptor levels inside the bandgap, leading to rich recombination paths for defect emission and extrinsic absorption. Impressively, the emission of donor-acceptor pair (DAP) in ZnIn_2S_4 can be significantly tailored by electrostatic gating due to efficient tunability of Fermi level (E_f). Furthermore, the layer-dependent dipole orientation of defect emission in ZnIn_2S_4 was directly revealed by back focal plane (BFP) imaging, where it presents obviously in-plane dipole orientation within a dozen layers thickness of ZnIn_2S_4 . These unique features of defects in ZnIn_2S_4 including extrinsic absorption, rich recombination paths, gate tunability and in-plane dipole orientation will definitely benefit to the advanced orientation-functional optoelectronic applications.

Keywords: ZnIn_2S_4 , defect, photoluminescence, back focal plane imaging, dipole orientation

Introduction

Atomically thin character of two-dimensional (2D) semiconductors makes them sensitive to intrinsic and extrinsic perturbations from thermal equilibrium, growth and processing, leading to the appearance of structural defects, including the vacancy, anti-site, edges and grain boundary.¹⁻³ These defects have great ability to strongly tailor the physical and chemical properties of 2D materials, which in turn enriches the functionalities of nano-devices. During the past years, many efforts⁴ have been taken to reveal the origin of defects in a representative of 2D semiconductors, transition metal dichalcogenides (TMDs), and the influence of defects on the electronic structure has been clearly revealed by microscopic⁵, spectroscopic^{3, 6, 7}, transport⁸⁻¹⁰ and ab initio techniques^{2, 11}. Defect engineering of ternary compounds is considered more promising than the widely studied binary TMDs, because ternary 2D systems have multiple degrees of freedom to tune their physical properties through stoichiometric variation and exhibits additional unique properties that binary 2D systems do not possess. Therefore, the investigation of ternary 2D systems via defect engineering is of great significance.

As a rediscovered layered semiconductor, ternary chalcogenide ZnIn_2S_4 has attracted broad interest due to their unique electronic structure and physical properties.¹²⁻¹⁴ On one hand, the presence of rich polymorphs in ZnIn_2S_4 endows it with a diverse range of fascinating performance. On the other hand, the direct bandgap with wide tunability in the visible spectrum and appropriate locations of conduction/valance bands make it promising for light-harvesting device applications,

such as photodetection¹⁵, solar cells¹⁶, light-emitting diodes¹⁷ and photocatalysis¹⁸. Similar to the case in ternary TMDs, defects have great influence on the physical properties of atomically thin character of 2D ZnIn₂S₄. For instance, it has been theoretically predicted that the introduction of S¹⁹ and Zn²⁰ vacancies leads to the formation of defect levels below the conduction band of ZnIn₂S₄. Experimentally, these vacancies can efficiently accelerate the separation of photo-generated electron-hole pairs, prolong the lifetime of carriers and dramatically improve the photocatalysis performance in defective ZnIn₂S₄ nanosheets and hybrid structures prepared by chemical approaches. Although the significance of defects in ZnIn₂S₄ has been accepted, the correlation between the origin of defects and physical properties of 2D ZnIn₂S₄ has not been clearly explored.

In this work, for the first time, we thoroughly studied the origin of defects in exfoliated monolayer and few-layer hexagonal ZnIn₂S₄, and their effects on the electronic structure and optical properties via versatile spectroscopic tools in combination with theoretical calculations. ZnIn₂S₄ exhibited the layer-dependent electronic bandgap and extrinsic absorption characteristics, the energy of which decrease by increasing the thickness. Moreover, the rich donor and acceptor levels inside the bandgap and the resultant complicate recombination paths of ZnIn₂S₄, such as band-to-band transition, donor-acceptor pair (DAP) recombination, acceptor-conduction band recombination were carefully distinguished by combining absorption, power and temperature dependent photoluminescence (PL), deep level transient spectroscopy (DLTS) with theoretical calculations. Besides, it is discovered that the

emission of DAP in ZnIn_2S_4 under the below-bandgap excitation can be significantly tailored by electrostatic gating due to the n -type semiconducting characteristics and efficient tunability Fermi level (E_f) of ZnIn_2S_4 . Finally, the layer-dependent dipole orientation of defect emission was directly revealed by back focal plane (BFP) imaging, which show obviously in-plane dipole orientation within a dozen layers thickness of ZnIn_2S_4 .

Results and Discussion

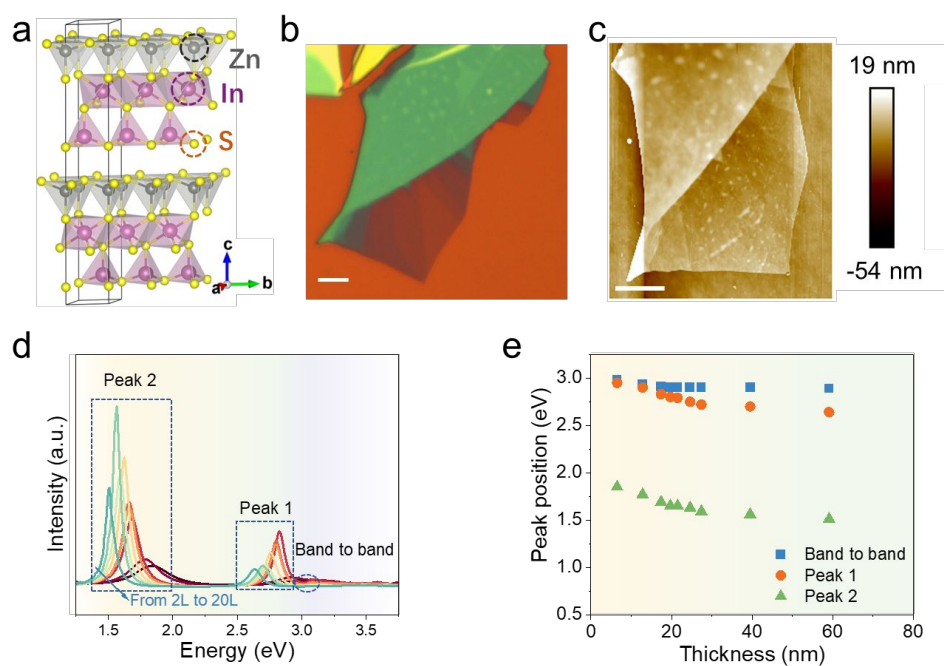


Figure 1. Electronic structure and layer-dependent absorption of ZnIn_2S_4 flakes. (a) Crystalline structure of hexagonal ZnIn_2S_4 . (b) Optical image and (c) AFM topography of a flake with different thicknesses. Scale bars in (b) and (c) is $5\ \mu\text{m}$. (d) Layer-dependent absorption of the flakes with different thicknesses. (e) Extracted layer-dependent intrinsic and extrinsic absorption peaks of ZnIn_2S_4 .

Figure 1a shows the crystalline structure of hexagonal ZnIn_2S_4 , which belongs to

P63mc space group with lattice constants of $a=3.85$ Å, $b=3.85$ Å and $c=24.68$ Å, respectively, the electronic structure of which was further verified by X-ray diffraction (XRD) and transmission electron microscopy (TEM) measurements (**Figures S1 and S2**). **Figure 1b** and **c** shows the optical image and AFM topography of a representative exfoliated flake with different thicknesses. The thickness of a monolayer ZnIn_2S_4 is determined to be 2.8 nm (**Figure S3**), in agreement with the theoretical value of ~ 2.5 nm. **Figure 1d** presents the layer dependent absorption spectra of ZnIn_2S_4 ranging from 2 L to ~ 20 L. The peak located at ~ 3 eV results from the intrinsic absorption while another two broad peaks (2.5 \sim 3 eV and 1.5 \sim 1.9 eV) correspond to the extrinsic absorption. The optical bandgap (E_g) of ZnIn_2S_4 with different thicknesses was extracted by using the Kubelka-Munk function, and the results shown in **Figures 1e** and **S4**. It is observed that the flakes exhibit the layer-dependent characteristics of electronic bandgap, where the bandgap of ZnIn_2S_4 decreases from 2.98 to 2.88 eV when the thickness changes from from 2 L to ~ 20 L. It is worth noting that the flakes exhibit strong extrinsic absorption, indicating that the defect levels inside the bandgap have great contributions to the photon absorption, which is quite different from the case in other 2D materials (such as MoS_2 , WSe_2) where the defect levels act as recombination paths, but have no contribution to absorption.²¹⁻²³

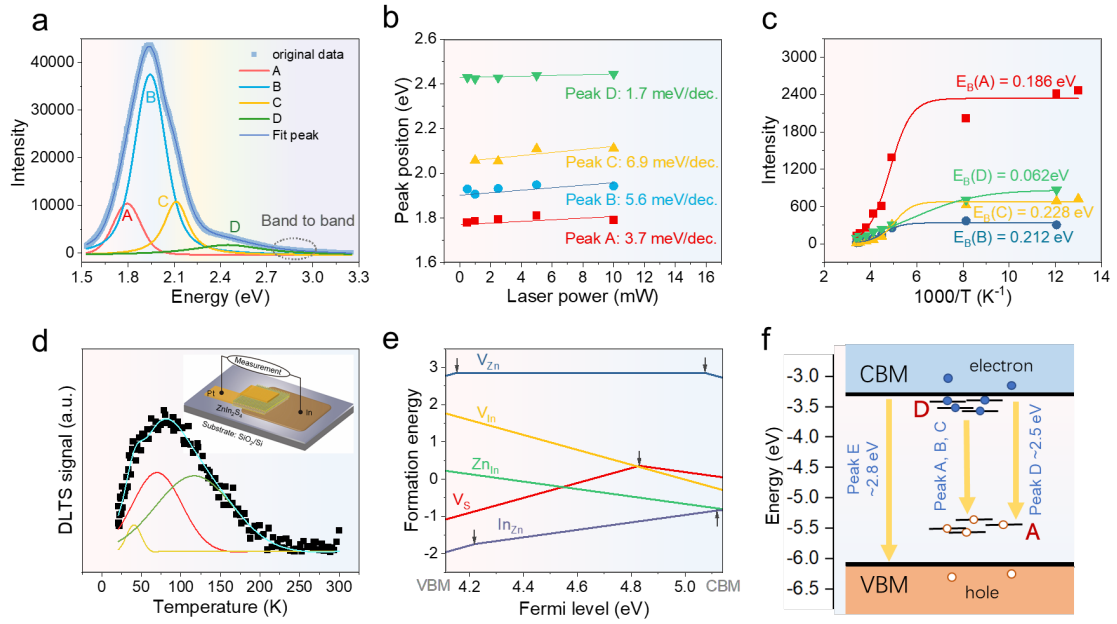


Figure 2. Photoluminescence performance by above bandgap excitation and rich recombination paths in ZnIn₂S₄ flakes. (a) Photoluminescence spectra at 300 and 77 K excited by 325 nm. (b) Integrated PL intensities of main peaks as a function of excitation power. (c) The integrated PL intensities of the four peaks (marked by A, B, C and D) as a function of temperature. (d) DLTS signal of a ZnIn₂S₄ device. Inset shows the schematics of an asymmetric ZnIn₂S₄ device for DLTS. (e) The formation energies of diverse point defect in ZnIn₂S₄. (f) Schematic diagrams of defect states inside the bandgap.

Given that luminescence can reflect the recombination behavior of defect states, we then studied the photoluminescence performance of the flakes. The flakes were excited with above-bandgap excitation via a laser wavelength of 325 nm (3.8 eV). **Figure 2a** shows the PL spectra of the flake at 300 K, where a wide peak at 1.6 ~ 2.9 eV and a shoulder (namely E) around 2.8 eV are observed. It is noted that this shoulder is more prominent at 77 K, which can be assigned to the band-to-band transition, consistent with the absorption characteristics. The broad PL peak at 300 K

was fitted by Voigt function, where four peaks located at 1.78, 1.91, 2.06, 2.43 eV (namely A, B, C, D) were observed (**Figure 2a**). To reveal the origin of the corresponding recombination paths, the power-dependent PL intensity of the peaks are extracted, as presented in **Figures 2b** and **S5**, and two features are observed. One is that the power-law index of all four peaks is lower than 1, suggesting that they are from the defect emissions. The other is that the energy of the peaks (A, B, C) appear blueshifts with increasing the power intensity, which is one of the characteristics of donor-acceptor pairs (DAP) recombination luminescence.²⁴

The peak energy for DAP recombination luminescence is expressed as

$$h\nu(R) = E_g - (E_D + E_A) + e^2/4\pi\epsilon R + f(R) \quad (1)$$

where E_g , E_D , and E_A are the band gap, the donor and acceptor ionization energies, respectively, R denotes the distance between the donor and acceptor defects, and ϵ is a static dielectric constant. Here, $-e^2/4\pi\epsilon R$ represents the Coulomb interaction energy between the donor and acceptor. In addition, $f(R) = \frac{-6.5e^2}{\epsilon_0 R} \left(\frac{a_B}{R}\right)^5$ represents the Van der Waals polarization between donor and acceptor, where a_B is the Bohr radius between donor and acceptor. With the increase of the excitation power, the resultant high density of excited charge carriers leads to a stronger Coulomb interaction between DAPs and a decrease in the distance between these defects. Consequently, DAP recombination luminescence energy shifts to higher energy when the excitation power density increases, as displayed in **Figure 2b**.

We further conducted the temperature-dependent PL measurements, and the results

are shown in **Figures 2c** and **S6**. It is observed that five peaks are clearly distinguished at low temperature. Given that the peak located at around 2.8 eV is assigned to be band to band transition, we focus on the broad peak at 1.5 ~ 2.5 eV. The integrated intensities of the four peaks as a function of temperature are shown in **Figure 2c**, and can be fitted by an Arrhenius equation²⁵:

$$I(T) = \frac{I_0}{1 + A \exp(-E_b / k_B T)} \quad (2)$$

where I_0 , E_b , k_B are the PL intensity at 0 K, the thermal activation energy, and the Boltzmann constant, respectively. The binding energy of the four peaks (peaks A to D) are determined to be 0.186, 0.212, 0.228 and 0.062 eV, respectively, large than the thermal energy (26 meV) at room temperature, further suggesting the strong charge trapping ability of defect levels. Given that ZnIn₂S₄ is n-type semiconductor, the acceptor level may be deeper than the donor level, and hence these obtained activation energies (peaks A to C) are considered as donor levels. Therefore, the donor levels extracted by photoluminescence behavior are determined to be 0.186, 0.212, and 0.228 eV below the conduction band minimum, respectively.

Apart from temperature-dependent PL measurements, Deep Level Transient Spectroscopy (DLTS) also serves as a valuable tool to reveal the defect levels in semiconductors.²⁶ A Schottky diode was fabricated, as depicted in the inset of **Figure 2d**, and the electrical performance are displayed in **Figure S7**. As shown in **Figure 2d**, the DLTS signal of ZnIn₂S₄ has a broadened peak, which represents the majority carrier (electron) trap in the material due to the n-type semiconducting characteristics of ZnIn₂S₄. By splitting the DLTS signal via Gaussian fitting, the temperature values

of the three peaks are 40, 69 and 117 K respectively, and the energy level positions of these three signal peaks are estimated to be located at 0.076, 0.138 and 0.243 eV below the conduction band, respectively. It is worth noting that the energy values of defect levels extracted from DLTS measurements is consistent with the values from temperature-dependent PL measurements, suggesting that at least three defect levels exist below the conduction band of ZnIn_2S_4 . According to the bandgap of ZnIn_2S_4 , DAP luminescence energy and the extracted donor levels, the acceptors levels are estimated to be 0.83, 0.68, 0.52 eV above the valence band maximum of ZnIn_2S_4 .

Next, we intend to explain the origin of defect levels (donors and acceptors) in ZnIn_2S_4 . It has been reported previously that bulk ZnIn_2S_4 with different polymorphs has rich intrinsic defects or disorders, especially vacancies and anti-structural defects (In-Zn exchange), leading to rich electron trapping levels and acceptors inside the bandgap of ZnIn_2S_4 . To further investigate whether these defects have contributions to the formation of energy levels inside the bandgap, we theoretically calculated the formation energies of vacancy (V_{Zn} , V_{S} , V_{In}) and anti-structural defects (Zn_{In} , In_{Zn}) by first-principles calculations with the accurate hybrid functions. **Figure 2e** shows the dependence of defect formation energies on chemical potential. It is worth noting that the calculated bandgap of ZnIn_2S_4 is estimated to be 1.12 eV, lower than the experimental value. It is found that Zn vacancy (V_{Zn}) is an amphoteric defect which can act as both acceptor with defect level at 0.042 eV above the VBM and donor at 0.068 eV below the CBM. However, the formation energy of V_{Zn} is largest, and hence Zn vacancy is not easy to exist. Regarding V_{In} defect, it has relatively low formation

energy without any defect-level in the bandgap. Compared with V_{Zn} and V_{In} , sulfur vacancy (V_S) acts as a deep donor with defect level at 0.31 eV below the CBM, while the formation energy of V_S is quite low under n-type condition, indicating that V_S is more likely to exist. Similarly, it is found that Zn_{In} creates no defect level inside the bandgap, whereas In_{Zn} is an amphoteric defect with an acceptor level (acceptor) at 0.11 eV above the VBM and a donor level at 0.02 eV below the CBM.

Experimentally, the anti-structural defects and S vacancies are observed from high-angle annular dark-field (HAADF) scanning transmission electron microscopy (STEM) and energy dispersive X-ray spectrometer (EDX) measurements, respectively, as shown in **Figures S8** and **S9**. According to the theoretical calculations above mentioned, these two kinds of defects can lead to the formation of energy levels inside the bandgap of $ZnIn_2S_4$, which is in agreement with previous reports about bulk counterparts²⁷⁻²⁹, where the intrinsic defects in bulk $ZnIn_2S_4$ induce exponentially distributed shallow donor states and acceptors. Therefore, in the following, we will explain the rich recombination paths, as depicted in **Figure 2f**. The D and A level indicate the donor and the acceptor levels originating from In_{Zn} defect respectively, while the deep level marked by S is attributed from the S vacancy. After above-bandgap excitation, there are several kinds of radiative recombination paths, marked by A to E (**Figure S6**). Peak E located at 2.75 eV is attributed to the band-to-band recombination, and peaks A-C is located at 1.6 ~ 2.5 eV for the DAP recombination (free electrons are captured by trap levels (D levels), and subsequently make radiative transitions to the A levels). Peak D at 2.5 eV is associated with the acceptor state

involved in the donor-acceptor luminescence transition that induces electron transition from the A levels to the CBM.

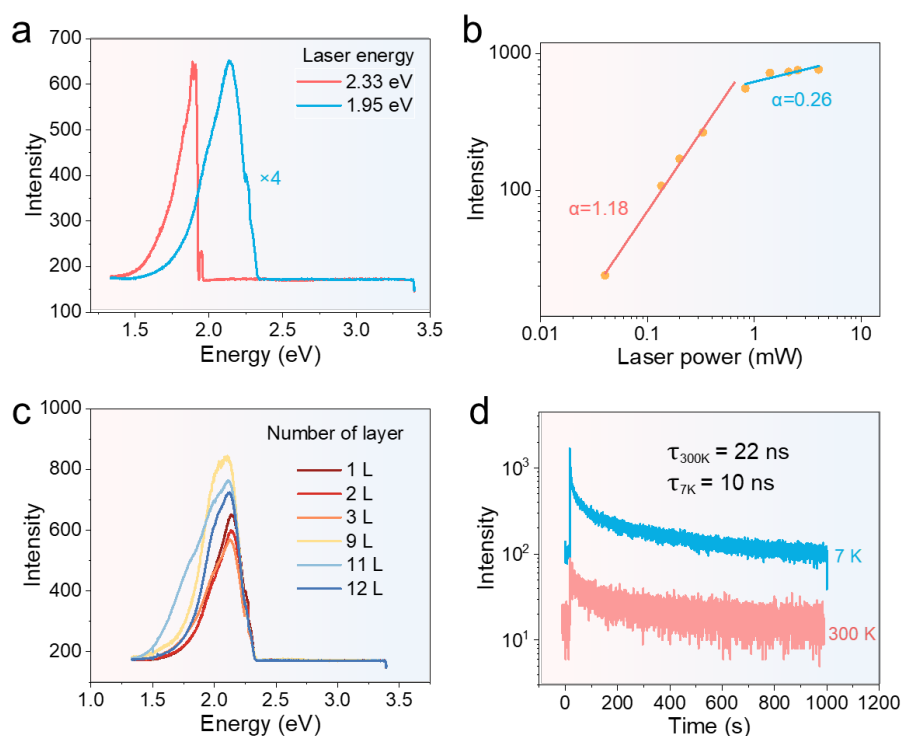


Figure 3. Photoluminescence performance of ZnIn_2S_4 flakes with below-bandgap excitation. (a) Wavelength-dependent PL spectra ZnIn_2S_4 . (b) Power-dependent PL spectra of ZnIn_2S_4 excited by laser energy of 2.33 eV. (c) Layer-dependent PL spectra and (d) Time-resolved PL of the flake at 7 and 300 K excited by ps laser with 2.33 eV.

As mentioned that the flake exhibits strong extrinsic absorption and defect emission, we then excited the flakes with below-bandgap excitation in order to further understand the origin of defects. **Figure 3a** shows the PL spectra of the flake with a thickness of 3-layer excited by a laser with wavelengths of 2.33 and 1.95 eV. It is found that the flake exhibits a wide peak under excitation by 2.33 and 1.95 eV, while the PL intensity excited by 1.95 eV is 4 times stronger than that excited by 2.33 eV. From the power-dependent PL spectra shown in **Figures S10** and **3b**, the power-law

behavior ($I = P^\alpha$) changes from superlinear ($\alpha = 1.18$) to sublinear ($\alpha = 0.26$) variation, and the PL intensity eventually saturates at large excitation power intensity. Given the feature of DAP recombination, where photoexcitation produces a non-ionized acceptor and possibly a non-ionized donor, the maximum value of α should be 2.²⁷ In our case, the value of α is less than 2, because not every photoexcited electron can be trapped by a specific donor-acceptor pair under excitation of 2.33 eV. At high excitation power intensity, due to the trap saturation, the carrier trapping and resultant DAP recombination are no longer effective for most free electrons, leading to the saturation of PL intensity. Therefore, under 2.33 eV excitation, the electrons can be excited from A level to the CBM or donor levels, and then captured by the traps, leading to the efficient DAP recombination. In contrast, the much lower PL intensity of ZnIn₂S₄ excited by 1.95 eV is due to inefficient excitation and trapping of carriers.

Whether the DAP recombination depends on the layer number of ZnIn₂S₄? **Figure 3c** shows the thickness-dependent PL of the flakes excited by 2.33 eV. With increasing the thickness from 2.8 to 36 nm, the PL peak energy exhibits a slightly redshift, suggesting that the energy levels of defects change slightly by the thickness. However, the intensities between different thickness from 2.8 to 36 nm without big change is shown in **Figure S11**. From the time-resolved PL (TRPL) results shown in **Figure 3d**, the lifetime of the peak located at 2.1 eV is estimated to be 22 and 10 ns at room temperature and 7 K. This ultra-long lifetime also confirms the characteristics of the defect emission.

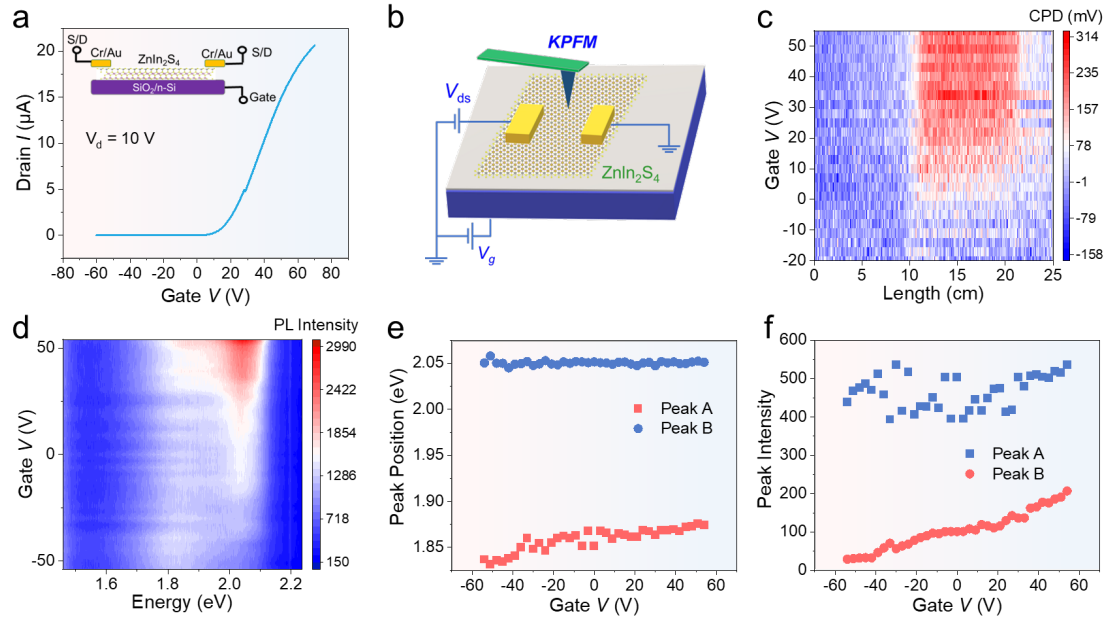


Figure 4. Gate-dependent electrical and optical performance of 8-layer ZnIn₂S₄ field effect transistor fabricated on SiO₂/Si substrate with Cr/Au electrode at room temperature. (a) FET performance of ZnIn₂S₄ device at room temperature with the thickness of 9-layer. Inset in (a) shows the schematic of the device. (b) Schematics of gate-dependent KPFM measurements. (c) Potential profiles along the channel at different gate voltage. (d) Gate-dependent PL intensity map at the power of 1.3 mW at 300 K with 2.33 laser excitation. (e) Peak positions and (f) peak intensities as a function of gate voltage.

Given the semiconducting characteristics of few-layer ZnIn₂S₄, we then studied its gate-dependent electrical and optical properties. **Figure 4a** shows the transfer curve of the device at a source-drain voltage of 10 V at room temperature, from which we found that the device presents electron-conduction characteristics with ON/OFF ratio up to 10⁷.

To further explore the gate-tunable E_f of ZnIn₂S₄, we carried out gate-dependent Kelvin probe force microscopies (KPFM) measurements. **Figure 4b** shows the

schematics of KPFM measurements, where both source and drain electrodes were grounded and V_g was applied on the heavily n-doped Si substrate. Surface potential profiles measured along Au-ZnIn₂S₄-Au under different V_g are shown in **Figure 4c**. Due to the difference in the work function between Au and ZnIn₂S₄, a gradual change in contact potential difference (CPD) is observed at Au-ZnIn₂S₄ junction. The surface potential of Au-ZnIn₂S₄-Au varies by gate voltages due to the presence of the unscreened long-range electrostatic interaction between the tip and V_g .^{30,31} It is worth noting that the surface potential of metals does not change with V_g , therefore, the relative difference in the CPD of Au-ZnIn₂S₄ (ΔV_{CPD}) can reflect the effect of V_g on the surface potential of ZnIn₂S₄. As can be seen in **Figure 4c**, ΔV_{CPD} increases significantly from 0 to 230 mV when V_g varies from -20 to 55 V, indicating that the E_f of the flake can be strongly tuned by electrostatic gating.

Considering the large E_f shift by electrostatic gating, we next investigated whether back gate voltage can control the spectral emission properties of ZnIn₂S₄. **Figure 4d** shows in a contour plot the photoluminescence intensity as a function of V_g with 2.33 eV excitation. The fitted peaks were selectively displayed in **Figure S12**. We clearly notice that the intensity increases monotonically as V_g decreases. The peak positions at different gate voltages are depicted in **Figure 4e**, where the peak energy exhibits a slight redshift with increasing the gate voltage, suggesting that the energy levels of defects are not sensitive to the electrical field. From **Figure 4f**, the peak intensities increase significantly with V_g increasing. It is evident that the electrical environment determines the activity of defect emission, due to defect stability modified by

changes to the local potential energy landscape induced by the applied voltage.³² It is well known that large donor and acceptor doping concentrations can lead to the intense DAP recombination.^{24, 33} In n-type ZnIn₂S₄ flake, the high electron density at donor states can be achieved due to the high energy level of E_f .³⁴ With increasing the gate voltages, the flake is more n-doped and generates high density at donor states, leading to the enhanced PL emission.

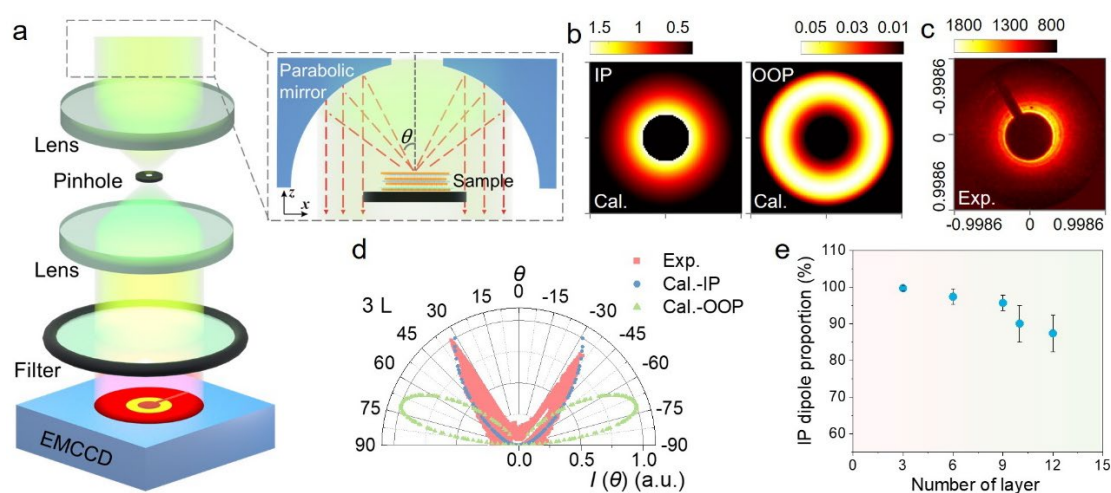


Figure 5. Thickness-dependent defect emission of the flakes via back focal plane imaging. (a) Schematics of BFP measurements. (b) Calculated and (c) experimental IP and OOP k-space emission patterns of the flakes with 3-layer thickness. (d) Measured and calculated far-field emission patterns as a function of the emission angle θ for the flakes in (b). (e) Layer-dependent in-plane dipole orientation proportion of ZnIn₂S₄ flakes.

Given that ZnIn₂S₄ has great potential for optoelectronic applications via defect engineering, it is of great importance to reveal the dipole orientation of defect emission. Back focal plane (BFP) and techniques help to measure wavevector distribution³⁵, where every point in the image plane corresponds to a distinct angle (θ)

of emission or the photo momentum along the certain θ ($k = k_0 \cdot n \cdot \sin(\theta)$), where n is the index of refraction and k_0 is the wave vector in air. **Figure 5a** shows the schematics of BFP measurements via parabolic mirror setup. The numerical aperture (NA) is 0.986, and more experimental details is described in method of supplementary information. An analytical model put forward by Andreas Lieb et al.³⁶ to simulate k -space emission pattern of ZnIn_2S_4 to confirm the dipole orientation in defect recombination. In order to test the accuracy of our measurement and analytical model, the dipole orientation of monolayer WSe_2 was measured shown in **Figure S13**, which is in consistent with its in-plane dipole characteristics.^{37, 38}

Figure 5b displays the calculated pure IP and OOP k -space emission patterns of the 3-layer flake, respectively, excited by 2.33 eV laser energy. From the emission patterns, it can be obviously observed that the intensity of OOP is about 30 times lower than IP pattern integrally, ascribing to the larger emission outcoupling of IP dipole.³⁹ Another feature is that the high intensity region scatters and forms a ring in OOP pattern while the IP pattern concentrates in the center albeit that there is a block (caused by sample holder) in the middle of the pattern, on account of the different field intensity distribution between the IP and OOP orientation.^{38, 40} **Figure 5c** shows the measured emission orientation in 3-layer ZnIn_2S_4 that could be appropriately recognized as IP dipole. **Figure 5d** draws normalized intensity along θ from the measured and calculated both IP and OOP k -space emission patterns for the flakes in **Figures 5b** and **c**, where the maximum intensity of measurement and simulation curves are at $\sim\theta = 30^\circ$ and intensity is gradually decreasing with the increase of θ ,

further confirming the IP orientation in fewer-layer ZnIn_2S_4 . Moreover, the layer-dependent emission orientation in ZnIn_2S_4 ranging from 2-layer to 14-layer was investigated, and the results are summarized in **Figures 5e** and **S14**, from which we conclude that the defect emission in ZnIn_2S_4 exhibits a mainly IP dipole component. This extrinsic absorption and IP dipole characteristics of defect states in few-layer ZnIn_2S_4 will definitely benefit to the advanced orientation-functional optoelectronic applications.

Conclusions

In summary, we have thoroughly investigated the origin of defects in mechanically exfoliated few-layer hexagonal ZnIn_2S_4 , and their effects on the electronic structure and optical properties. ZnIn_2S_4 exhibited the layer-dependent bandgap and extrinsic absorption characteristics. Secondly, we discussed the abundant donor and acceptor levels of ZnIn_2S_4 inside the bandgap and carefully distinguished the resultant complicate recombination paths of band-to-band transition, donor-acceptor pair (DAP) recombination and acceptor-conduction band recombination. Besides, it is revealed that the E_f of *n*-type ZnIn_2S_4 semiconductor has efficient gate tunability, and the emission of DAP in ZnIn_2S_4 can be significantly controlled by static electric gating even under laser excitation below the bandgap. Finally, through the back focal plane (BFP) imaging, it directly revealed that layer-dependent dipole orientation of defect emission, determining the almost pure IP orientation within a dozen layers thickness of ZnIn_2S_4 in aspect of defect emission. Our work demonstrates the great ability to tune the unique physical properties of 2D ternary semiconductors via defect

engineering for multifunctional optical and optoelectronic applications in the future.

References

1. Rasool, H. I.; Ophus, C.; Zettl, A. *Advanced Materials* **2015**, *27*, (38), 5771-5777.
2. Hu, Z. H.; Wu, Z. T.; Han, C.; He, J.; Ni, Z. H.; Chen, W. *Chem Soc Rev* **2018**, *47*, (9), 3100-3128.
3. Jeong, T. Y.; Kim, H.; Choi, S. J.; Watanabe, K.; Taniguchi, T.; Yee, K. J.; Kim, Y. S.; Jung, S. *Nature Communications* **2019**, *10*.
4. Hong, J. H.; Jin, C. H.; Yuan, J.; Zhang, Z. *Advanced Materials* **2017**, *29*, (14).
5. Xiong, Z. X.; Zhong, L.; Wang, H. T.; Li, X. Y. *Materials* **2021**, *14*, (5).
6. Tebyetekerwa, M.; Zhang, J.; Xu, Z.; Truong, T. N.; Yin, Z. Y.; Lu, Y. R.; Ramakrishna, S.; Macdonald, D.; Nguyen, H. T. *Acs Nano* **2020**, *14*, (11), 14579-14604.
7. Zhou, M. F.; Wang, W. H.; Lu, J. P.; Ni, Z. H. *Nano Research* **2021**, *14*, (1), 29-39.
8. Qiu, H.; Xu, T.; Wang, Z.; Ren, W.; Nan, H.; Ni, Z.; Chen, Q.; Yuan, S.; Miao, F.; Song, F. *Nature communications* **2013**, *4*, (1), 1-6.
9. Jariwala, D.; Sangwan, V. K.; Late, D. J.; Johns, J. E.; Dravid, V. P.; Marks, T. J.; Lauhon, L. J.; Hersam, M. C. *Applied Physics Letters* **2013**, *102*, (17), 173107.
10. Han, M. Y.; Brant, J. C.; Kim, P. *Physical review letters* **2010**, *104*, (5), 056801.
11. Wu, F.; Smart, T. J.; Xu, J. Q.; Ping, Y. *Phys Rev B* **2019**, *100*, (8).
12. Lappe, F.; Niggli, A.; Nitsche, R.; White, J. G. *Zeitschrift für Kristallographie-Crystalline Materials* **1962**, *117*, (1-6), 146-152.
13. Yang, R.; Mei, L.; Fan, Y.; Zhang, Q.; Zhu, R.; Amal, R.; Yin, Z.; Zeng, Z. *Small Methods* **2021**, *5*, (10), 2100887.
14. Ran, J.; Zhang, H.; Qu, J.; Shan, J.; Davey, K.; Cairney, J. M.; Jing, L.; Qiao, S. Z. *Small* **2021**, *17*, (32), 2100296.
15. Zhen, W. L.; Zhou, X.; Weng, S. R.; Zhu, W. K.; Zhang, C. J. *Acs Applied Materials & Interfaces* **2022**, *14*, (10), 12571-12582.
16. Pourabdollah, M.; Zeynali, H.; Akbari, H. *Mater Lett* **2017**, *196*, 312-315.
17. Ko, M.; Yoon, H. C.; Yoo, H.; Oh, J. H.; Yang, H.; Do, Y. R. *Advanced Functional Materials* **2017**, *27*, (4).
18. Zou, P.; Su, G. K.; Li, Z. G.; Li, Y. Z.; Zhou, T. Y.; Kang, Y. K. *Colloid Surface A* **2022**, 633.
19. Zhang, S. Q.; Zhang, Z. F.; Si, Y. M.; Li, B.; Deng, F.; Yang, L. X.; Liu, X.; Dai, W. L.; Luo, S. L. *Acs Nano* **2021**, *15*, (9), 15238-15248.
20. Jiao, X. C.; Chen, Z. W.; Li, X. D.; Sun, Y. F.; Gao, S.; Yan, W. S.; Wang, C. M.; Zhang, Q.; Lin, Y.; Luo, Y.; Xie, Y. *Journal of the American Chemical Society* **2017**, *139*, (22), 7586-7594.
21. Castellanos-Gomez, A.; Quereda, J.; van der Meulen, H. P.; Agrait, N.; Rubio-Bollinger, G. *Nanotechnology* **2016**, *27*, (11).
22. Lin, T. N.; Santiago, S. R. M.; Caigas, S. P.; Yuan, C. T.; Lin, T. Y.; Shen, J. L.; Chen, Y. F. *Npj 2d Mater Appl* **2019**, *3*.
23. Aslan, O. B.; Deng, M. D.; Heinz, T. F. *Phys Rev B* **2018**, *98*, (11).
24. Aihara, N.; Tanaka, K.; Uchiki, H.; Kanai, A.; Araki, H. *Applied Physics Letters* **2015**, *107*, (3).
25. Li, Y.; Wang, T.; Wang, H.; Li, Z.; Chen, Y.; West, D.; Sankar, R.; Ulaganathan, R. K.; Chou, F.; Wetzel, C. *Nano letters* **2018**, *18*, (8), 5078-5084.
26. Ci, P.; Tian, X.; Kang, J.; Salazar, A.; Eriguchi, K.; Warkander, S.; Tang, K.; Liu, J.; Chen, Y.;

- Tongay, S. *Nature communications* **2020**, 11, (1), 1-8.
27. Crandles, D.; Charbonneau, S.; Fortin, E.; Anedda, A. *Solid State Commun* **1985**, 56, (4), 367-370.
28. Serpi, A. *Journal of Physics D: Applied Physics* **1976**, 9, (13), 1881.
29. Guzzi, M.; Grilli, E. *Materials chemistry and physics* **1984**, 11, (3), 295-304.
30. Li, Y.; Xu, C.-Y.; Zhang, B.-Y.; Zhen, L. *Applied Physics Letters* **2013**, 103, (3), 033122.
31. Xu, B.; Li, Y.; Sun, Z. Y.; Zhao, Z.; Yang, L.; Gao, F.; Hu, P. A.; Zhen, L.; Xu, C. Y. *Adv Electron Mater* **2021**, 2100584.
32. Chakraborty, C.; Kinnischtzke, L.; Goodfellow, K. M.; Beams, R.; Vamivakas, A. N. *Nat Nanotechnol* **2015**, 10, (6), 507-U38.
33. Aydinli, A.; Gasanly, N. M.; Goksen, K. *J Appl Phys* **2000**, 88, (12), 7144-7149.
34. Pei, J. J.; Gai, X.; Yang, J.; Wang, X. B.; Yu, Z. F.; Choi, D. Y.; Luther-Davies, B.; Lu, Y. R. *Nature Communications* **2016**, 7.
35. Vasista, A. B.; Sharma, D. K.; Kumar, G. **2018**.
36. Lieb, M. A.; Zavislan, J. M.; Novotny, L. *J Opt Soc Am B* **2004**, 21, (6), 1210-1215.
37. Xiao, K.; Yan, T. F.; Cui, X. D. *Acs Nano* **2020**, 14, (1), 1027-1032.
38. Luo, Y.; Liu, N.; Kim, B.; Hone, J.; Strauf, S. *Nano Letters* **2020**, 20, (7), 5119-5126.
39. Brotons-Gisbert, M.; Proux, R.; Picard, R.; Andres-Penares, D.; Branny, A.; Molina-Sanchez, A.; Sanchez-Royo, J. F.; Gerardot, B. D. *Nature Communications* **2019**, 10.
40. Schuller, J. A.; Karaveli, S.; Schiros, T.; He, K. L.; Yang, S. Y.; Kymissis, I.; Shan, J.; Zia, R. *Nat Nanotechnol* **2013**, 8, (4), 271-276.

Supplementary Information for

Defect emission and its dipole orientation in layered ternary ZnIn₂S₄ semiconductor

Rui Wang^{1,Δ}, Quan Liu^{3,Δ}, Sheng Dai⁵, Chao-Ming Liu^{1,7}, Yue Liu¹, Zhao-Yuan Sun¹,
Hui Li⁴, Chang-Jin Zhang⁴, Han Wang^{5,*}, Cheng-Yan Xu⁵, Wen-Zhu Shao^{1,*}, Alfred J.
Meixner³, Dai Zhang^{3,*}, Yang Li^{1,2,*} and Liang Zhen^{1,2,6}

¹ *School of Materials Science and Engineering, Harbin Institute of Technology, Harbin 150001, China*

² *MOE Key Laboratory of Micro-Systems and Micro-Structures Manufacturing, Harbin Institute of Technology, Harbin 150080, China*

³ *Institute of Physical and Theoretical Chemistry, Eberhard Karls University Tübingen, Tübingen 72076, Germany*

⁴ *School of Physical Science and Technology, Center for Transformative Science, ShanghaiTech University, Shanghai 201210, China*

⁵ *Institutes of Physical Science and Information Technology, Anhui University, Hefei 230601, China*

⁶ *Sauvage Laboratory for Smart Materials, School of Materials Science and Engineering, Harbin Institute of Technology (Shenzhen), Shenzhen 518055, China*

⁷ *Laboratory for Space Environment and Physical Sciences, Harbin Institute of Technology, 150001 Harbin, China*

E-mails: liyang2018@hit.edu.cn (Y.L.); wzshao@hit.edu.cn (W.Z.S.); wanghan3@shanghaitech.edu.cn (H.W.); dai.zhang@uni-tuebingen.de (D.Z.)

Methods

Sample preparation. ZnIn_2S_4 flakes were obtained by mechanical exfoliation from single crystals. The Bulk ZnIn_2S_4 was grown by a chemical vapor transport method (CVT)¹. The few-layer samples were mechanical exfoliated on SiO_2/Si substrate with 280 nm thickness SiO_2 . The few-layers were judged by optical microscope (*Imager A2m, Zeiss*), and the number of layers were determined by AFM (*Dimension Icon-PT, Bruker*).

Structural and morphology characterization. The structure was carried out by powder X-ray diffraction (*Empyrean*) with Cu $K\alpha$ radiation. The TEM measurements were conducted in *talos f200x* with 200 KV acceleration voltage. The HAADF-STEM was performed by spherical aberration corrected transmission electron microscope (AC-TEM, *FEI Themis Z*) with 80 KV acceleration voltage. The samples for TEM and AC-TEM were on the microgrid copper mesh using wetting-enabled-transfer.

The morphology characterization was proceeded in AFM through *Scanasyt* mode with *Scanasyt air* tip, where the samples were mechanical exfoliated on SiO_2/Si substrate with 280 nm thickness SiO_2 . Morphology and element distribution was analysed by scanning electron microscopy (SEM, *SUPRA55*) equipped with energy dispersive X-ray detector (EDX, *Oxford*), where the sample was prepared on conductive tape.

Characterization of optical performance. The microscopic absorption spectra and optical images were collected in a home-designed spectroscopy system (Gora-UVN-FL, built by Ideaoptics, Shanghai, China), with a Xeon light source between 300 nm and 1100 nm. The power-dependent and temperature-dependent PL excited by a laser with energy of 3.82 eV was carried out by *LabRAM HR Evolution*, integrated with a liquid nitrogen cryostat (*Linkam*).

The BFP was measured by a home-built scanning confocal microscope, the luminous emitted from sample were reflected by parabolic mirror². The light passed through confocal system (consists of two tube lens with focal of 100 mm and a pinhole of 100 μm) and then across the filter to remove the laser energy. Finally, the BFP image was collected at electron multiplying charge coupled device (EMCCD).

DLTS measurement. The DLTS was performed using the *Phystech FT-1230* system. The DLTS deduces the defect level properties by measuring the response of the capacitance to temperature using Schottky device. The initial bias is -5 V. The capacitance transients (ΔC) were measured with a 1 MHz DLTS spectrometer operated with a temperature scan from 20 K to 300 K with a step of 2 K. The reverse bias voltage and the pulse voltage were -5 V and 0 V, respectively. The pulse width (T_w) during the test was 1.92 ms.

DFT calculation. Calculations were performed using Vienna Ab initio Simulation Package (VASP), based on density function theory (DFT). A $4 \times 4 \times 1$ supercell with 224 atoms was employed for all calculations. The exchange-correlation effect was described within the generalized gradient approximation in the Perdew–Burke–Ernzerhof (PBE) functional and the van der Waals (vdW) interaction was described with the DFT-D3 method. Projector-augmented wave method was used to describe the interaction between ion cores and valence electrons. Plane-waves kinetic energy cutoff was set to 400 eV for geometry optimization and the total energy convergence criterion of 10^{-6} eV is adopted. The optimized convergence criterion for atomic coordinates was less than 0.01 eV/Å for forces on each atom. The $1 \times 1 \times 1$ Monkhorst–Pack k-meshes were used to sample the Brillouin zone for all structures presented in this study. For total energy calculation, Heyd-Scuseria-Ernzerhof (HSE06) hybrid functional was applied and the

kinetic energy cutoff was set to 300 eV.

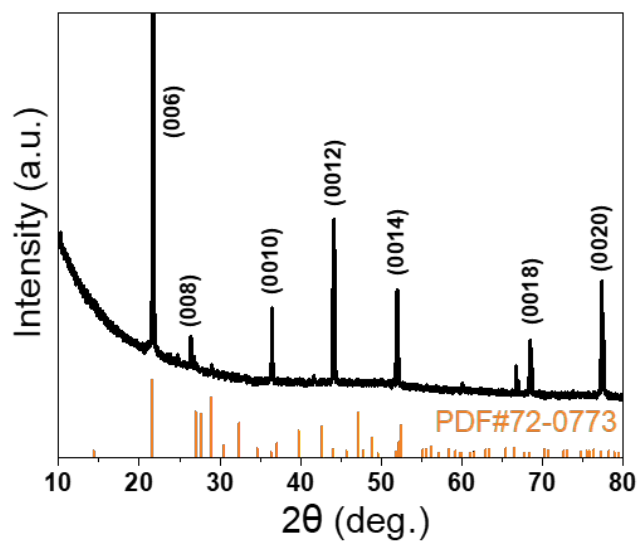


Figure S1. X-ray diffraction of bulk ZnIn_2S_4 by θ - 2θ scanning.

Only the (00 l) reflections show up in the diffractogram, suggesting single [001] out-of-plane orientation. Diffraction pattern indicates that the flake is a single crystal with hexagonal structure (ICDD card no.72-0773)

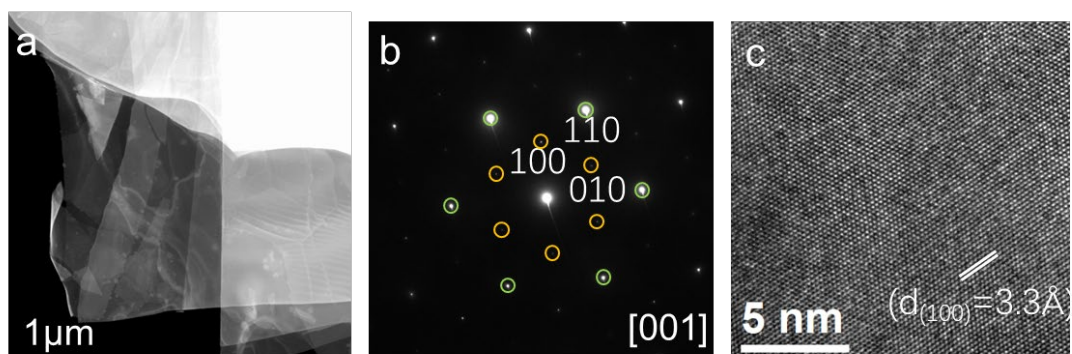


Figure S2. (a) Low-magnification TEM image, (b) the corresponding selected area electron diffraction (SAED) pattern and (c) high-resolution TEM of ZnIn_2S_4 flake.

SAED patterns distribute alternating light and dark, where dark dots are circled by yellow and light dots are circled by green. It is because that the reciprocal lattices show extinction of reflections hkl with $-h+k+l \neq 3n$, which indicates that it exhibits an ordered hexahedral structure³. From the high-resolution TEM image of few-layer ZnIn_2S_4 , the lattice spacing of (100) is measured to be 3.3 Å.

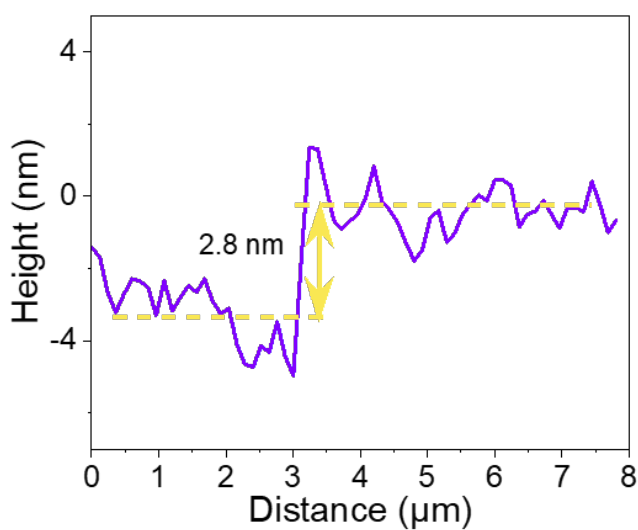


Figure S3. Height profile of monolayer ZnIn_2S_4 flake in Figure 1c. The single layer was measured as 2.8 nm, consistent with the theoretical value of 2.5 nm.

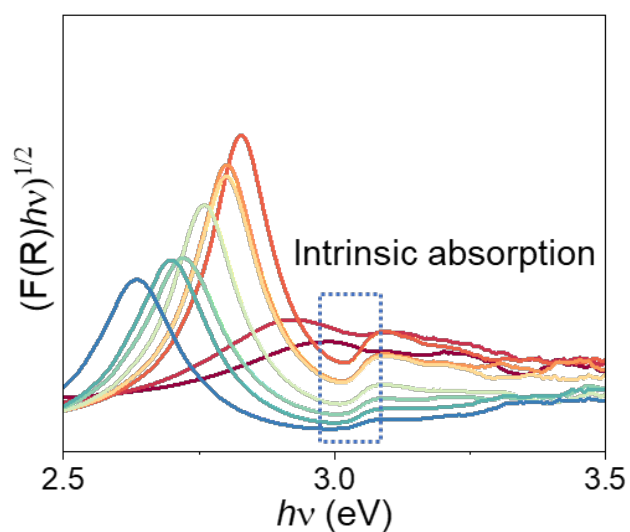


Figure S4. thickness-dependent optical absorption spectra of ZnIn₂S₄ flakes. The bandgap of ZnIn₂S₄ flakes were determined by using the Kubelka-Munk function.

We extracted the optical bandgap (E_g) from the optical absorption spectra by using the Kubelka-Munk function since the ZnIn₂S₄ has a direct band gap: $[F(R_\infty)hv]^{0.5}=A(hv-E_g)$. The intersection of the tangent with the x-axis can give a good approximation of the E_g values of the samples, estimating to be 2.88~2.98 eV from 2 L to ~20 L

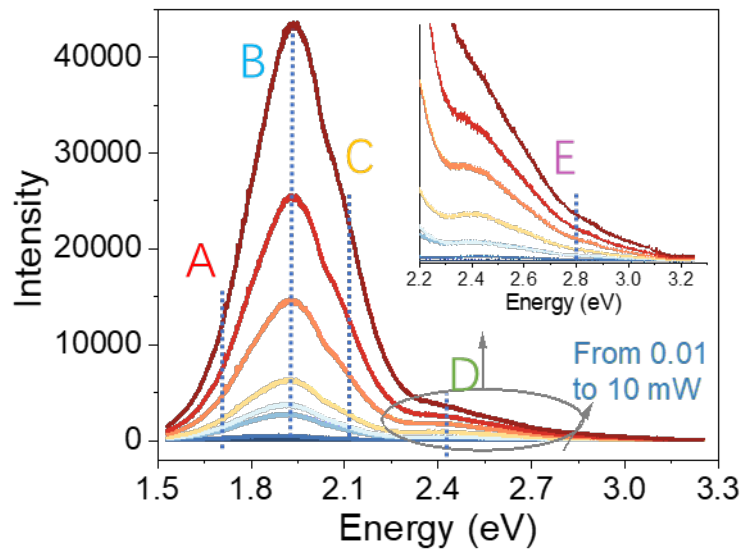


Figure S5. Power-dependent photoluminescence spectra of the ZnIn₂S₄ flake from 0.01 to 10 mW laser power with 4 extrinsic peak (A-D) and weak intrinsic peak (E).

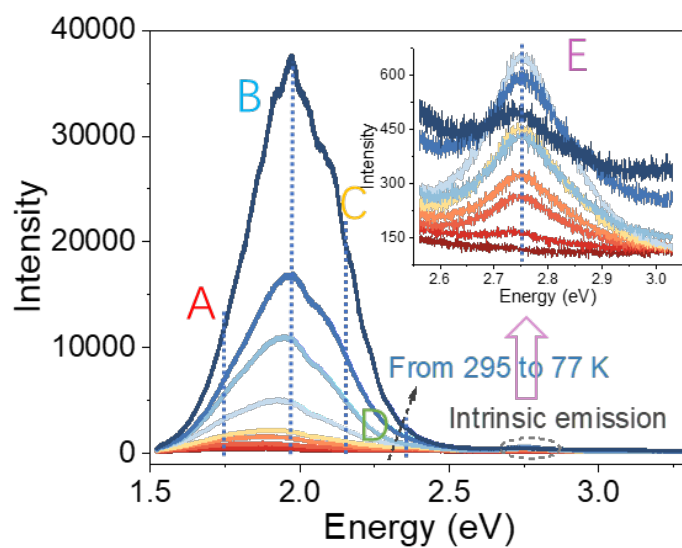


Figure S6. Temperature-dependent PL spectrum of the ZnIn_2S_4 flake, from which the intensity is increase with the decrease of temperature from 295 k to 77 k.

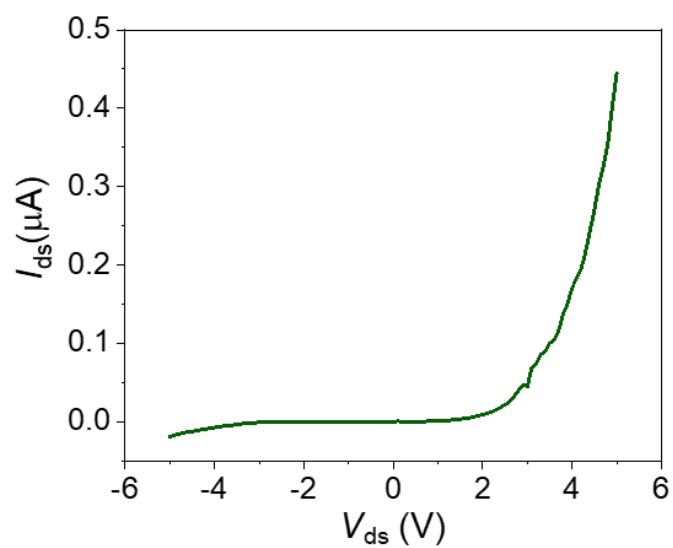


Figure S7. Electrical performance of ZnIn_2S_4 Schottky diode fabricated by indium and platinum metal electrode at room temperature.

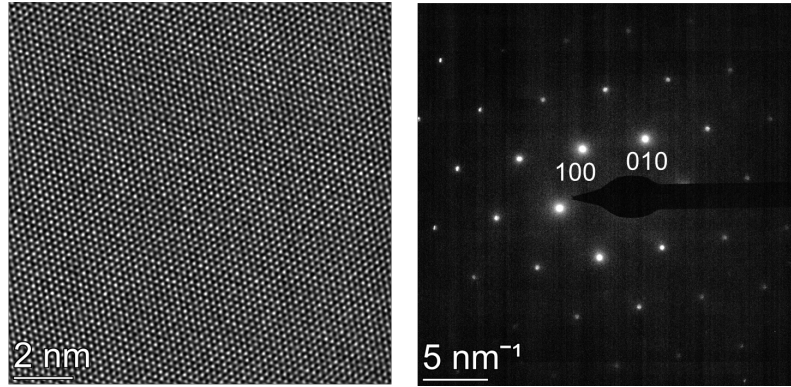


Figure S8. An AC-STEM measurements of ZnIn_2S_4 . The left is quasi-disordered⁴ distribution which mainly refers to the random distribution of In, Zn atom in local area, and the right is the corresponding SAED patterns.

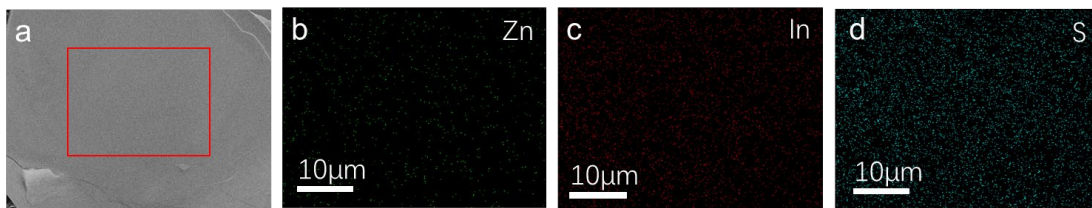


Figure S9. (a) Morphology and (b-d) EDS mapping of ZnIn_2S_4 flake under SEM with the atomic ratio of Zn, In, S, is approximately 1.22: 2: 3.78.

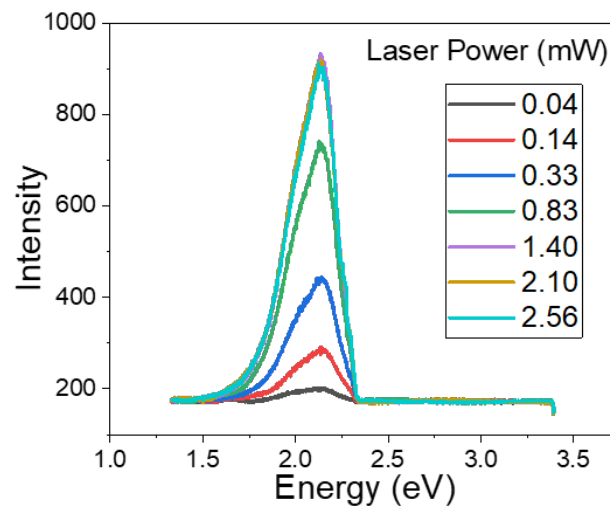


Figure S10. Power-dependent PL spectra of ZnIn₂S₄ with 3-layer under excitation of 2.33 eV laser energy at room temperature.

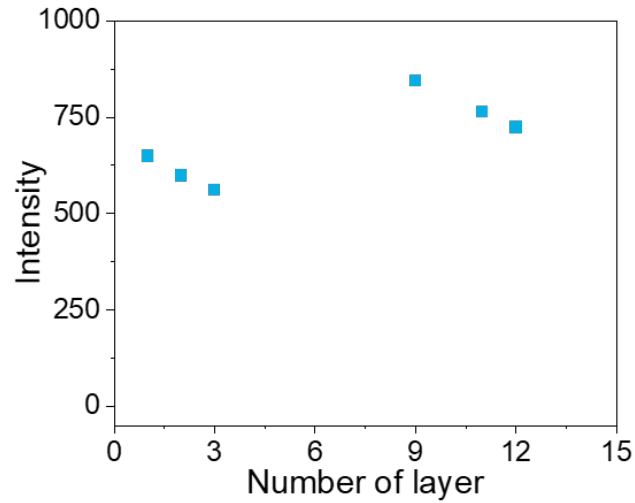


Figure S11. The PL intensity varied from 1-layer to 12-layer under excitation of 2.33 eV laser energy with the power of 0.83 mW.

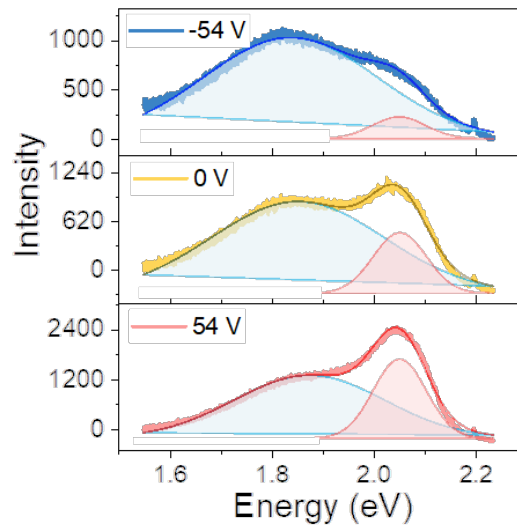


Figure S12. The selectively fitted result of PL spectra at gate voltages of -54, 0 and 54 V under the excitation of 2.33 eV laser energy. Two peaks are located at ~1.8 and ~2.1 eV, respectively.

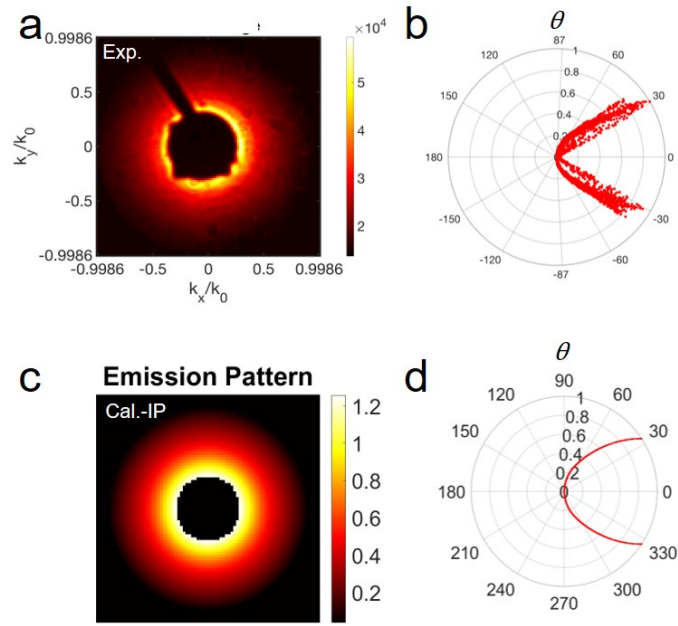


Figure S13. The measured IP orientation of k -space emission pattern (a) and a function of the emission angle θ (b) of monolayer WSe₂. (c) and (d) are the corresponding calculated results.

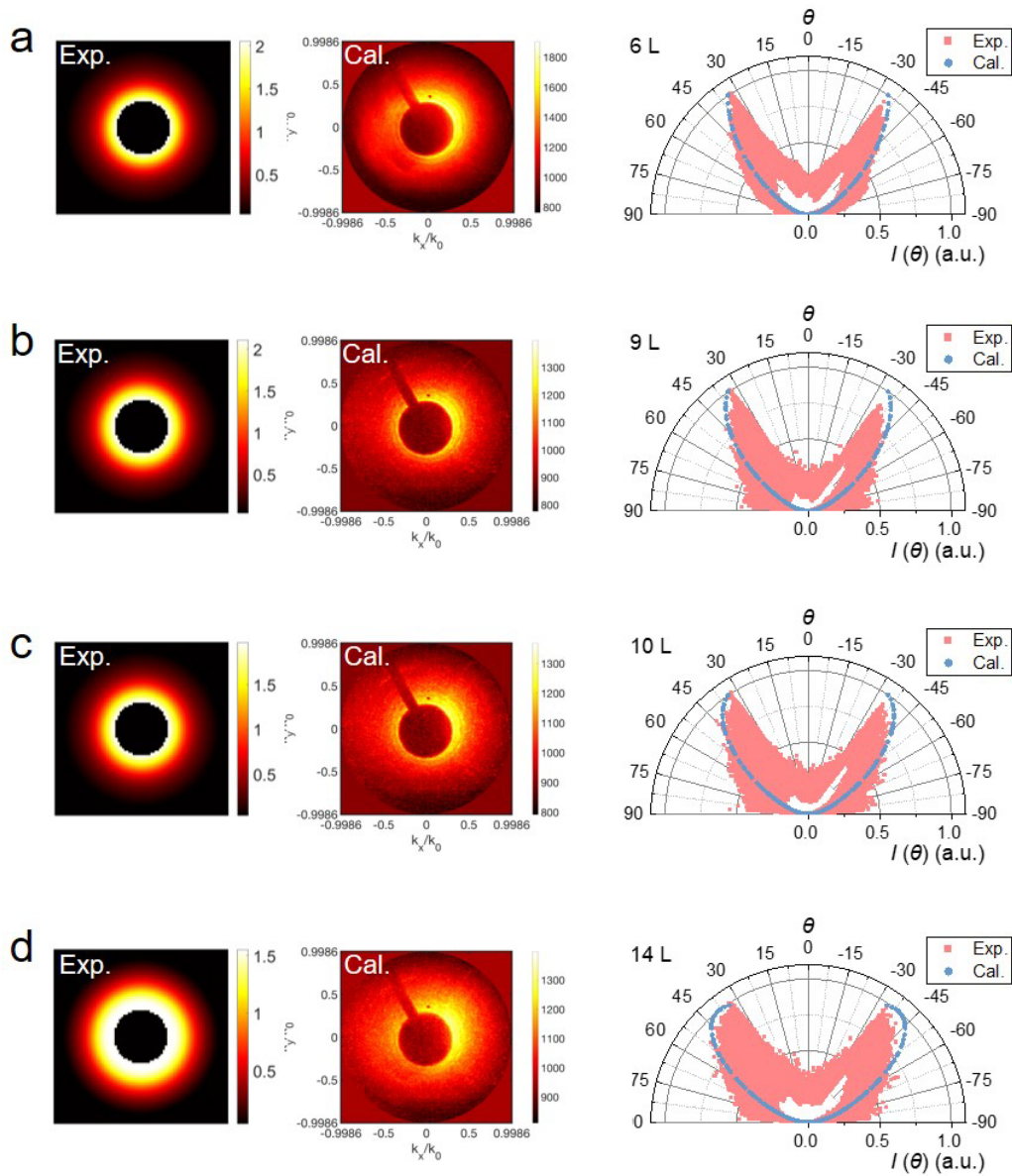


Figure S14. Thickness-dependent k -space emission patterns of measured and calculated images from defect emission with flakes of (a) 6-layer, (b) 9-layer, (c) 10-layer and (d) 14-layer.

Reference

1. Weng, S. R.; Zhen, W. L.; Li, Y. D.; Yan, X.; Han, H.; Huang, H.; Pi, L.; Zhu, W. K.; Li, H.; Zhang, C. J. *Phys Status Solidi-R* **2020**, 14, (7).
2. Lieb, M. A.; Meixner, A. J. *Opt Express* **2001**, 8, (7), 458-474.
3. Anagnostopoulos, A. N.; Manolikas, C.; Papadopoulos, D. *physica status solidi (a)* **1983**.
4. Bosacchi, A.; Bosacchi, B.; Franchi, S.; Hernandez, L. *Solid State Commun* **1973**, 13, (11), 1805-1809.